Research Square

Preprints are preliminary reports that have not undergone peer review.
They should not be considered conclusive, used to inform clinical practice,
or referenced by the media as validated information.

ZnO-functionalized sugarcane bagasse biochar for enhanced photocatalytic removal of paracetamol: structural, optical, and interfacial charge-transport properties

Erik S. Pereira
Federal University of Itajubá
Ralf R. R. Junior
ralf.junior@unifei.edu.br
Federal University of Itajubá
Adhimiar F. Oliveira
Federal University of Itajubá
Sandro J. Andrade
Federal University of Itajubá

Research Article

Keywords: ZnO, biochar nanocomposite, Photocatalysis, Paracetamol removal, Interfacial charge transfer, Sugarcane bagasse biochar

Posted Date: November 10th, 2026

DOI: https://doi.org/10.21203/rs.3.rs-11367322/v1

License: This work is licensed under a Creative Commons Attribution 4.0 International License.
Read Full License

Additional Declarations: No competing interests reported.

ZnO-functionalized sugarcane bagasse biochar for enhanced photocatalytic removal of paracetamol: structural, optical, and interfacial charge-transport properties

Erik S. Pereira[a], Ralf R. R. Junior[a], Adhimiar F. Oliveira[a] and Sandro J. Andrade[a]*

[a] Institute of Physics and Chemistry, Federal University of Itajubá, 3500-903, Minas Gerais, Brazil

*Corresponding author. E-mail: ralf.junior@unifei.edu.br

ABSTRACT

Functionalized semiconductor/carbon nanocomposites offer promising opportunities for photocatalytic environmental remediation by combining pollutant adsorption with enhanced charge separation and transport. In this work, we synthesized a ZnO-functionalized biochar composite (ZnO@BC) by thermally converting zinc hydroxychloride anchored onto a sugarcane bagasse-derived carbonaceous framework. X-ray diffraction and scanning electron microscopy coupled with energy-dispersive spectroscopy confirmed the formation of crystalline hexagonal wurtzite ZnO nanostructures, with an average crystallite size of approximately 28.9 nm, distributed throughout the porous biochar matrix. Nitrogen adsorption–desorption analysis revealed a predominantly microporous structure with a specific surface area of 74.15 $m^2 g^{-1}$. The optical band gap decreased slightly from 3.22 eV for commercial ZnO to 3.18 eV for ZnO@BC, while the Urbach energy decreased from 110.3 ± 1.6 to 49.3 ± 0.8 meV, indicating reduced optical disorder in the composite. Electrochemical impedance spectroscopy revealed an 11.7% increase in low-frequency conductance under illumination, consistent with enhanced photoinduced charge transport through the ZnO/biochar interface. The ZnO@BC composite achieved 78.5% paracetamol removal after 60 min of irradiation, with an apparent pseudo-first-order rate constant of 0.0207 min^{-1}, compared with 43% removal and 0.0079 min^{-1} for commercial ZnO. Radical-scavenging experiments indicated relevant contributions from hydroxyl and superoxide radicals, with a secondary contribution from photogenerated holes. The results demonstrate that integrating ZnO with sugarcane bagasse biochar provides a functional hybrid interface with enhanced photocatalytic performance and promising potential for pharmaceutical-contaminant removal.

Keywords: *ZnO/biochar nanocomposite. Photocatalysis. Paracetamol removal. Interfacial charge transfer. Sugarcane bagasse biochar.*

INTRODUCTION

Photocatalytic Advanced Oxidation Processes (AOPs) have emerged as a promising strategy for the oxidative degradation of recalcitrant organic pollutants into environmentally benign molecules [1,2]. Zinc oxide (ZnO) has been extensively investigated as an efficient n-type semiconductor photocatalyst owing to its strong oxidizing potential, non-toxicity, and high catalytic reactivity [3]. However, the practical application of pristine ZnO nanoparticles is severely restricted by their wide band gap (~3.21 eV), rapid photogenerated electron-hole (e-/h+) recombination, and low surface adsorption capacity [4]. These limitations have motivated the development of functionalized ZnO-based materials that combine the semiconductor with a second phase capable of modifying surface interactions and charge-transport pathways. In this context, biochar derived from agricultural residues has attracted considerable interest as a carbonaceous support for photocatalytic materials [9–11]. Its porous structure, surface functional groups, and carbon-based electronic network can promote pollutant adsorption while providing pathways for photoinduced charge transport [11].

Although various ZnO/biochar composites have been reported, the synthesis route plays a decisive role in determining the crystalline morphology, interfacial charge transfer, and overall photocatalytic stability [3]. Conventional synthesis approaches often rely on organic surfactants, complex templates, or multi-step hydrothermal methods that leave organic residues and complicate operational scale-up [5,6]. In this context, the thermal conversion of inorganic layered precursors, such as zinc hydroxychloride (ZHC, $Zn_5(OH)_8Cl_2.H_2O$), represents a template-free and highly scalable alternative to generate crystalline ZnO nanostructures with controlled defect distribution [7]. However, the direct integration of ZHC-derived ZnO onto sugarcane bagasse biochar, together with a systematic assessment of the resulting optical and interfacial charge-transport properties during photocatalysis, remains insufficiently explored. The impacts of supporting ZnO into biochar can also modify the interfacial charge transport and narrow the effective optical bandgap [8].

In this study, a ZnO-functionalized sugarcane bagasse biochar composite (ZnO@BC) was synthesized through the template-free thermal conversion of ZHC deposited onto a sugarcane bagasse-derived carbonaceous framework. The resulting material was structurally and morphologically characterized by X-ray diffraction (XRD), scanning electron microscopy coupled with energy-dispersive spectroscopy (SEM-EDS), and nitrogen adsorption–desorption analysis. Its optical properties and photoinduced charge-transport behavior were investigated through optical spectroscopy, electrochemical impedance spectroscopy (EIS), and transient photocurrent measurements. The photocatalytic

performance of ZnO@BC was evaluated using paracetamol as a model pharmaceutical contaminant, including kinetic analysis, reactive-species scavenging experiments, and reuse tests. The results are discussed by correlating the structural and interfacial properties of the functionalized nanocomposite with its photocatalytic performance, providing insights into the role of the ZnO/biochar interface in pharmaceutical-contaminant degradation.

2 EXPERIMENTAL

2.1 MATERIALS

The sugarcane bagasse was collected from a local market in Itajubá, Minas Gerais, Brazil. Zinc Chloride salt was purchased from Dinâmica Química Contemporânea® (purity >97%). P-benzoquinone was purchased from Sigma-Aldrich® (purity >98%). Sodium Hydroxide (purity >97%) was purchased from Synth®. Methanol (LS Chemicals; purity >99,0%). EDTA was purchased from Synth® (purity> 99.0%). PCT (purity >98%) was sourced from a compounding pharmacy (Itajubá, Minas Gerais, Brazil) and used as received without any further purification.

2.2 METHODS

2.2.1 Synthesis of sugarcane bagasse biochar functionalized with ZnO

Sugarcane bagasse collected from the local market in Itajubá, Minas Gerais, Brazil, was washed with distilled water. The impregnation of 6,8164 g of biomass was approached with the co-precipitation of ZHC into the biomass, by the dropwise addition of 100.0 mL of $ZnCl_2$ solution (0.5 mol L^{-1}). The pH value was adjusted by the addition of NaOH (1.0 mol L^{-1}), to keep pH=8 in the synthetic process, for 2 hours of synthesis. The resulting biomass impregnated with ZHC was filtered, washed with distilled water and dried in oven furnace, at 60 ºC for 24h.

After drying process, the resulting material was placed into a porcelain crucible and placed in a muffle furnace for the thermal treatment, at 500 ºC for 5 h, to achieve the thermal conversion of ZHC into ZnO, as represented in previous reports [9,10]. As result, the functionalized ZnO@BC was obtained, characterized and applied in photocatalytic degradation of PCT in aqueous solutions.

2.2.2 Structural Characterization

The prepared biochar was characterized by Fourier Transform Infrared Spectroscopy, FT-IR with attenuated total reflectance module (Spectrum 100, PerkinElmer®) from 650 cm^{-1} to 4000 cm^{-1}, with 16 scans; X-ray Diffraction, XRD (X'pert PRO, PANalytical®) from 10º to 80º of 2θ, 0.02º s^{-1} (with Cu X-ray source), and Scanning Electron Microscopy with Energy Dispersive Spectroscopy, SEM-EDS (EVO-MA 15, Zeiss®). The Scherrer's equation was applied to assess the average ZnO crystallite size, as represented below in Eq. 1:

$$D = \frac{K\lambda}{\beta cos(\theta)} \quad (1)$$

Where D is the crystallite size, K represents the Scherrer constant (adopted as K=0.90 in this case); λ is the corresponding wavelength of the X-ray source (0.15406 nm), β is the full width at half maximum in each crystallographic peak and θ is the Bragg's angle of each crystallographic peak. Surface characterization was performed with N_2 adsorption-desorption analysis using the BET methodology (QuantumChrome Nova Station A®).

2.2.3 Optical Characterization

The optical characterization of ZnO@BC was performed through diffuse reflectance spectroscopy (DRS) in Ocean SR spectrometer (Ocean Optics®). The resulting measurements were analyzed according to the Kubelka-Munk equation as represented in Eq 2:

$$F(R) = \frac{(1-R)^2}{2R} \quad (2)$$

The optical bandgap energy was subsequently estimated using the modified Tauc relation, as represented in Eq. 3.

$$[F(R)hv]^n = A\left(hv - E_g\right) \quad (3)$$

Where $F(R)$ is the Kubelka-Munk function, hv represents the incident photon energy, A represents a constant of energy-independent proportionality, E_g is the optical band gap of the material. In this work, $n = 2$ was adopted, once ZnO represents a direct gap semiconductor. Also, the conduction band and valence band energy were estimated from Mulliken electronegativity theory, with Eqs. 4 and 5.

$$E_{VB} = X - E_e + \frac{1}{2}E_g \quad (4)$$

$$E_{CB} = E_{VB} - E_g \quad (5)$$

where X is the absolute electronegativity of ZnO (5.79 eV), E_e is the energy of free electrons on the hydrogen scale (~4.5 eV vs. NHE), and E_g is the experimentally determined optical bandgap.

2.2.4 Photoelectrochemical characterization

The ZnO@BC composite was pressed into a pellet, and electrical contacts were prepared using silver conductive paint. The resulting pellet was used as the working electrode for the photoelectrochemical measurements.

Electrochemical impedance spectroscopy (EIS), measurements were carried out by employing an AUTOLAB potentiostat with NOVA 2.1 software for parameter adjustment. EIS measurements were carried out in

the dark and under blue-light-emitting diode (LED) illumination over a frequency range of 0.1~Hz to 1~MHz at open-circuit potential.

2.2.5 Photocatalytic removal of PCT from water

The PCT removal experiments were performed with the objective of assessing the different mechanisms in the contaminant removal from aqueous medium. In this scenario, the experiments were planned to assess the effects of the absence of light (and the contribution of sorption processes) and irradiation with a near-UV Hg light source (emission spectrum presented in Fig. S1, Supporting Information).

All the experiments, made in triplicate, were conducted with 0.25 g L^{-1} of the ZnO@BC catalyst in an aqueous solution of PCT (1.0 mg L^{-1}) in a photoreactor with a magnetic stirrer, using a Hg vapor lamp at 15 cm from reaction beaker. Initially, samples were collected from the experimental sets before the addition of the catalyst, at an initial time (t_{-30}). After the addition of the catalyst, the experiments considered an initial 30 minutes-adsorption experiment, with samples collected after 15 and 30 minutes in the absence of light (t_{15} and t_{30}). Then the light source was turned on for a 60-min experiment, which samples were collected in $t_{35,}$ $t_{40,}$ $t_{60,}$ t_{75} and $t_{90.}$

The collected samples were analyzed in HPLC-DAD, using C_{18} column (XRD-C18, Agilent ®), with isocratic elution using methanol and water (proportion of 30:70 v/v), with chromatographic flow of 0,5 mL min^{-1} and injection with 20 µL. The maximum absorbance of PCT was set to 243 nm. Control experiments with commercial ZnO nanoparticles (ZnO NPs) were performed following the methods described above. To evaluate the kinetics of PCT removal, the experimental data obtained during the photocatalytic with ZnO NPs and ZnO@BC assays were fitted to the non-linear PFO model. The fitting was performed using the concentration values determined by HPLC at each sampling interval, and the kinetic rate (k_1) were compared with commercial ZnO NPs to assess the PCT degradation behavior under the investigated experimental conditions. Mineralization of PCT was evaluated using a Total Organic/Inorganic Carbon analyzer (N/C AnalytikJena 2100 S) by determining the change in inorganic carbon (IC) relative to the initial PCT concentration (1.0 mg L^{-1}).

2.2.6 Scavenging Experiments

Photocatalytic experiments were conducted in the presence of scavengers to investigate the contribution of the main reactive species involved in PCT degradation. Methanol (10 mmol L^{-1}), *p*-benzoquinone (1.0 mmol L^{-1}), and

ethylenediaminetetraacetic acid (EDTA, 1.0 mmol L^{-1}) were used as scavengers for hydroxyl radicals ($HO^{\bullet}$), superoxide radicals ($O_2^{\bullet-}$), and photogenerated holes (h^+), respectively [11,12].

The experiments were carried out under the same conditions described for the photocatalytic assays. A catalyst concentration of 0.25 g L^{-1} (ZnO@BC) was adopted in a 1.0 mg L^{-1} PCT solution. The specific scavenger was added to the reaction medium prior to the addition of the catalyst. The suspension was stirred magnetically in the dark for 30 min to establish adsorption-desorption equilibrium, and an initial aliquot was collected after adsorption-desorption equilibrium (t_0). followed by irradiation with a light source for 60 min. A final sample was taken after 60 minutes of light exposure in each quenching experiment. All collected samples were filtered through 0.45 μm PTFE syringe filters (Millex-LCR) and analyzed by HPLC-DAD.

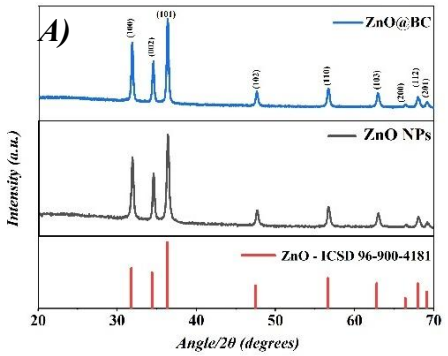
3 RESULTS AND DISCUSSION

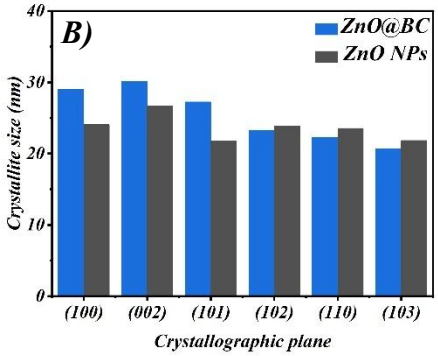
3.1 Material Structural and Optical Characterization

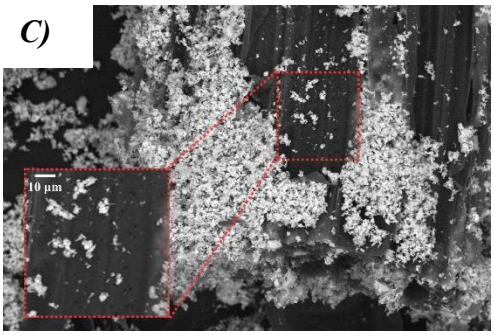
The crystallographic characterization of ZnO@BC composite agrees with ZnO commercial and ZnO ICSD chart, as shown in Fig. 1a. The identification of the (100), (002), and (101) crystallographic planes, typical of ZnO with a hexagonal wurtzite-type structure, along with secondary signals such as (102), (110), (103), (200), (112), and (201) found in ZnO-based materials, indicates the successful conversion of the precursor synthesized ZHC into ZnO [9]. The resulting ZnO aggregates can be associated with the synthetic process, once the OH^-/Zn^{2+} ratio seems to morphologically impact the ZHC particles. As reported by Cousy *et al*., OH^-/Zn^{2+} ratios over 2.0 lead to the formation of aggregates of ZHC [13]. Once aggregated, the thermal conversion of ZHC into ZnO can be reached at temperatures above 400 ºC [9]. The crystallite sizes of ZnO@BC and pristine ZnO NPs, calculated via the Scherrer equation across the main crystallographic planes (100), (002), (101), (102), (110), and (103), presented remarkably similar values ranging between 20 and 30 nm (Fig. 1c). This similarity indicates that the thermal conversion of zinc hydroxychloride directly on the sugarcane bagasse biochar matrix did not hinder the crystallization process or induce excessive grain growth. The oxygenated functional groups on the biochar surface likely provided well-dispersed nucleation sites, confining the growth of ZnO crystallites and preventing sintering during calcination. Consequently, the composite retained nanoscale dimensions comparable to commercial nanoparticles, ensuring a high density of active catalytic sites while benefiting from the structural support and enhanced electron mobility provided by the biochar framework

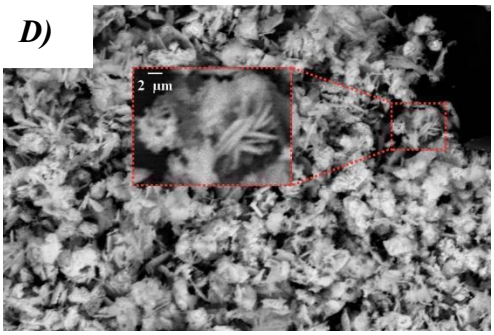
The observed ZnO occurrences in Fig. 1d can be associated to nanometric rods, as previously reported in literature [14]. Furthermore, the characteristic pores of the BC, resulting from the pyrolysis process, can also be observed in

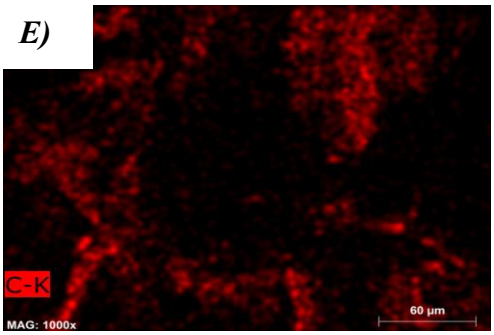
Fig. 1c and in Fig. S2 (Supporting Information). The average particle size, according Sherrer's equation, resulted in average of 28.9 nm. Although, it is noticeable the aggregation of ZnO after thermal treatment, as seen in Fig. 1b, resulting in aggregates of rod-like structures, under the size of 1.0 μm. The semi quantification, represented in Fig.1 and Table S1, also agrees with the regions containing the BC and the anchored ZnO, representing the lightened portion in Fig. 1c, associated to Zn and O portions (Figs. 1h and 1f, respectively). Additionally, Fig. 1e refers to the region containing C atoms derived from the pyrolyzed biomass, whereas Fig. 1g refers to a region containing a low amount of Chlorine atoms, possibly associated to remaining precursor anions atoms from the synthetic process.

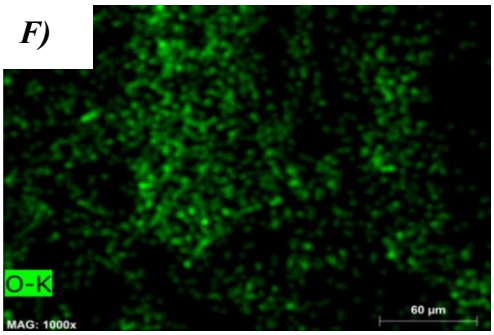

A)
ZnO@BC
ZnO NPs
ZnO - ICSD 96-900-4181
Intensity (a.u.)
Angle/2θ (degrees)
20
30
40
50
60
70

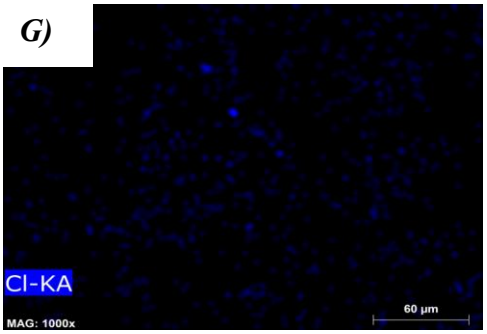

B)
ZnO@BC
ZnO NPs
Crystallite size (nm)
0
10
20
30
40
(100)
(002)
(101)
(102)
(110)
(103)
Crystallographic plane


C)
10 µm


D)
2 µm


E)
C-K
MAG: 1000x
60 µm


F)
O-K
MAG: 1000x
60 µm


G)
Cl-KA
MAG: 1000x
60 µm

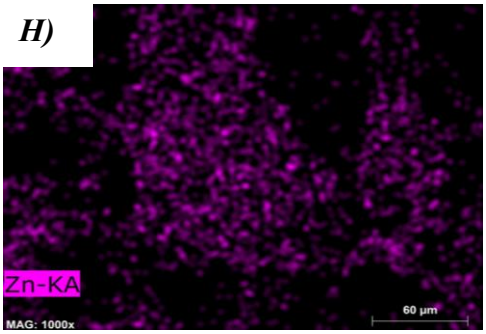

H)
Zn-KA
MAG: 1000x
60 µm

Fig. 1. ZnO@BC characterization: (A) XRD comparison between synthesized ZnO@BC, commercial ZnO and ICSD card for ZnO (96-900-4181); (B) comparative size between ZnO@BC and Commercial ZnO NPs; SEM micrographs at 1000x (C) and 5000x (D); EDS determination for carbon (E), for oxygen (F), for chlorine (G), and for zinc (H).

The resulting adsorption isotherm from BET analysis is represented in Fig.2, which can be classified as Type IV-a, according to IUPAC classifications. Textural properties were also obtained through N_2 adsorption-desorption studies. Analysis via the t-method reveals that micropores contribute significantly to the material's total surface area, accounting for 64.28 m^2/g (approximately 86.7% of the total area) and a micropore volume of 0.0251 cm^3/g (roughly 60.5% of the total pore volume). The predominant microporosity is inherently attributed to the biochar (BC) carbonaceous framework [15]. Simultaneously, the creation of mesoporous channels (external surface area of 9.87 m^2/g) originates from the anchoring and spatial distribution of ZnO nanoparticles onto the biochar surface.

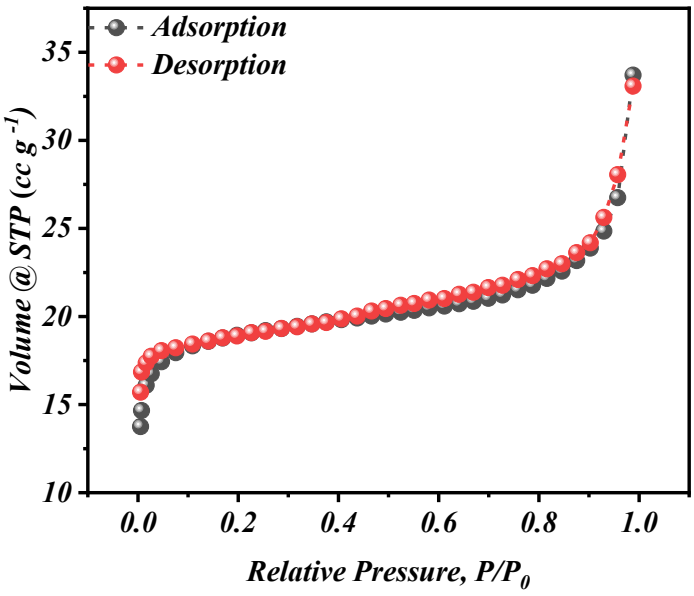


Fig. 2. N_2 Adsorption-desorption Isotherm for BC@ZnO.

Table 1. N_2 physisorption data obtained from surface properties characterization.

Parameter	Value	Method
Surface Area	74.151 $m^2 g^{-1}$	MultiPoint BET
Total Pore Volume	0.0415 $cm^3 g^{-1}$	Single point ($P/P_0 = 0.957$)
Average pore diameter	2.238 nm	4V/A (BET)/ BJH
Micropore Volume	0.0251 $cm^3 g^{-1}$	t-method
Micropore surface Area	64.28 $m^2 g^{-1}$	t-method
External Surface Area	9.87 $m^2 g^{-1}$	t-method

As summarized in Table 1, the ZnO@BC composite exhibits a specific surface area of 74.15 $m^2 g^{-1}$, with a total pore volume of 0.0415 $cm^3 g^{-1}$ and an average pore diameter of 2.24 nm. The pore size distribution confirms a micro-mesoporous hybrid network, where the average pore diameter sits precisely at the boundary of the mesoporous regime (2–50 nm).

The optical band gap energy of the synthesized photocatalysts was evaluated using the Kubelka-Munk plot method (Fig. 3a). The optical bandgap shift from 3.22 eV in commercial ZnO to 3.18 eV in the ZnO@BC composite confirms the creation of localized shallow intragap states near the band edges, driven by the interfacial interaction between the semiconductor and the functionalized carbonaceous framework. Concurrently, a marked reduction in Urbach energy was recorded for the composite ($E_U = 49.3 \pm 0.8$ meV) relative to the commercial reference (110.3 ± 1.6 meV), as represented in Fig. 3b. This sharp contrast indicates that while commercial particles exhibit significant structural disorder and deep trap sites acting as non-radiative recombination centers, the carbonaceous-template guides an oriented crystallization process [16]. Consequently, the ZnO@BC composite achieves an optimized state for photocatalysis as it extends the optical absorption coupled with minimized deep-trap recombination.

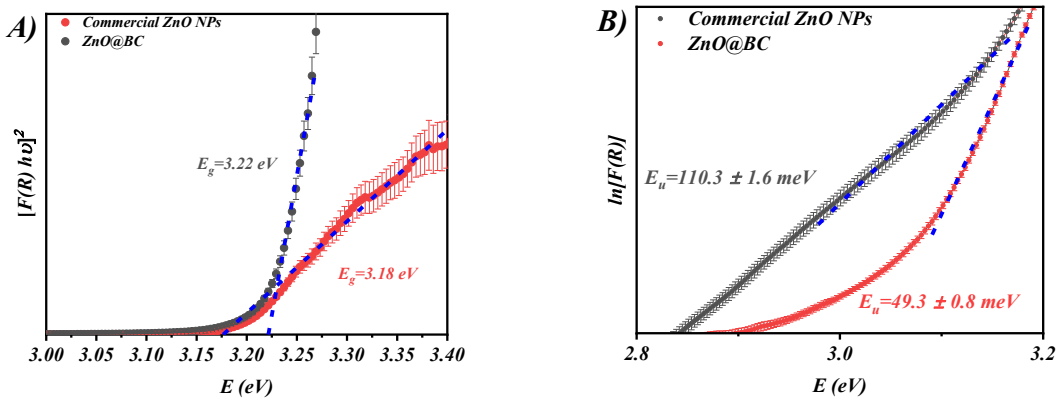


Fig. 3. Optical characterization: (a) Kubelka-Munk plot of ZnO NPs and ZnO@BC; (b) Urbach energy calculation.

To further elucidate the band alignment and charge transfer thermodynamics, the valence band (VB) and conduction band (E_{CB}) edge potentials were calculated via Mulliken's electronegativity theory, adopting an absolute electronegativity χ of 5.79 eV for ZnO. The resulting conduction and valence band energies showed a shift of ±0.02 V, as represented in Table 2. The theoretical approximation of the energy of the conduction band suggests that $O_2^{\bullet-}$ can be thermodynamically generated, once the reduction potential of molecular oxygen is -0,16 V vs NHE.

Table 2. Theoretical approximation of Mulliken's theory to determine the energy of conduction and valence bands of commercial ZnO and ZnO@BC.

Parameter	**Commercial ZnO NPs**	**ZnO@BC**
Conduction band energy	-0.32 V vs NHE	-0.30 V vs NHE
Valence band energy	+2.90 V vs NHE	+2.88 V vs NHE

3.2 Impedance Spectroscopy and Electrical Response Modeling

The electrical response of the ZnO@BC composite was investigated via electrochemical impedance spectroscopy (EIS) under dark and illuminated conditions (Fig. 4). To accurately represent the physical processes, an admittance-based approach considering two parallel power-law terms (associated with Constant Phase Elements, CPEs) Eq. 6 was applied:

$$Y(\omega) = Q_a(j\omega)^{na} + Q_\beta(j\omega)^{nb} \quad (6)$$

where Q_a and Q_b are the admittance pseudo-capacitance parameters, na and nb are the dispersion exponents, and w is the angular frequency. The complex impedance is obtained via Z(w) = 1 / Y(w). This power-law formulation aligns with Jonscher's universal dielectric response [17], capturing both the low-frequency conductive contribution and the high-frequency dispersive process. The experimental impedance spectra were verified for causality and stability using Kramers-Kronig relations [18].

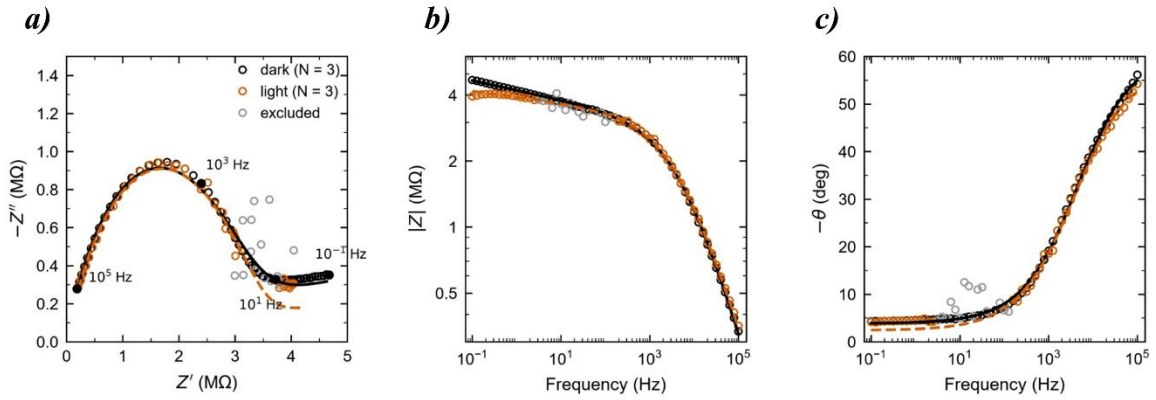


Fig. 4. Impedance spectra of the ZnO@BC composite under dark (black) and illuminated (orange) conditions: (a) Nyquist plots, (b) Bode magnitude plots, and (c) Bode phase angle plots. Symbols represent experimental data; grey points indicate noise-excluded data.

As summarized in Table 3, the fitting parameters reveal distinct physical behaviors in the two frequency regimes. The first exponent (n_a ~ 0.02 - 0.04) approaches zero, representing a predominantly conductive channel, whereas the second exponent (n_β ~ 0.65 - 0.68) indicates a more dispersive charge-transport response, consistent with localized or hopping-like carrier dynamics [17].

Illumination predominantly modulates the low-frequency conductive contribution. Upon light exposure, the low-frequency conductance (G_a, evaluated at 0.1 Hz) increases by 11.7%, from 214.7 ± 0.6 nS in the dark to 239.8 ± 1.5 nS under light. Concurrently, the crossover frequency (f×) shifts downward from 4.42 ± 0.06 kHz to 3.77 ± 0.14 kHz. The photoinduced increase in (Ga) is consistent with enhanced charge-carrier transport under illumination and indicates that photogenerated carriers contribute to the low-frequency electrical response of the composite.

Table 3. Parameters obtained from the fitting of the ZnO@BC impedance response under dark and illuminated conditions.

Parameter	Dark	Light – main fit	Light – all points
n_a	0.0429 ± 0.0006	0.0266 ± 0.0014	0.0325 ± 0.0023
n_b	0.678 ± 0.002	0.650 ± 0.004	0.659 ± 0.008
$f_×$ (kHz)	4.42 ± 0.06	3.77 ± 0.14	4.28 ± 0.24
$C_β$ @ 10 kHz (pF)	8.25 ± 0.03	8.12 ± 0.06	8.01 ± 0.10
G_a @ 0.1 Hz (nS)	214.7 ± 0.6	239.8 ± 1.5	235.6 ± 2.5
χ^2_{red}	9.0 x 10^{-5}	3.8 x 10^{-4}	1.3 x 10^{-3}

The dispersive contribution was comparatively less sensitive to illumination, with (nb) changing only slightly from 0.678 to 0.650 and (Cb) remaining nearly constant at approximately 8.1 pF. Thus, the relatively small changes in the high-frequency parameters suggest that the main photoinduced effect is associated with the low-frequency conductive response rather than with a substantial modification of the underlying dispersive relaxation process.

These electrical results are consistent with the optical characterization of ZnO@BC. The lower Urbach energy ((E_U = 49.3) meV) indicates a reduced contribution of band-tail disorder relative to the commercial ZnO reference, while the small decrease in the estimated optical band gap ((E_g = 3.18) eV) suggests a modest modification of the optical absorption edge after incorporation of ZnO into the biochar matrix. Together with the increase in low-frequency conductance under illumination, these results support the interpretation that the ZnO@BC architecture modifies the charge-transport response of ZnO and facilitates photoinduced carrier transport. However, direct conclusions regarding carrier recombination or trap-mediated processes would require complementary techniques specifically sensitive to these phenomena.

3.3 PCT photocatalysis and reusability

The application of ZnO@BC allowed the comparison with commercial ZnO in the photocatalytic degradation of PCT, with results represented in Fig. 5a. Firstly, the ZnO@BC composite showed a better adsorption-desorption yield until equilibrium was reached, in comparison with the commercial ZnO NPs, being coherent with biochar's porous

nature, which is represented in micrographs in Fig.S1, which improves the PCT interactions with the heterogeneous solid phase.

Under irradiation, ZnO@BC achieved 78.5% removal of PCT within 60 min, compared with 43.0% for commercial ZnO NPs under the same experimental conditions. This enhanced removal can be associated with the synergistic combination of PCT adsorption by the porous biochar matrix and photocatalytic transformation at the ZnO/biochar interface [19].

The kinetic behavior of PCT photocatalytic degradation over ZnO@BC composite and commercial ZnO NPs was further evaluated using the non-linear pseudo-first-order kinetic model (Fig. 5b). As represented in Fig. 5b, the non-linear fitting demonstrated excellent agreement with the experimental data, yielding high determination coefficients (R^2 = 0.99163 for ZnO@BC and R^2= 0.89725 for pristine ZnO NPs. The calculated apparent kinetic rate constant k_1 for ZnO@BC (0.0207min^{-1}) was noticeably higher than that obtained for commercial ZnO NPs (0.00791min^{-1}), indicating a significant enhancement in reaction kinetics. This accelerated degradation rate is primarily attributed to the synergistic effect between the sugarcane bagasse biochar framework and the anchored ZnO nanoparticles. The porous carbonaceous matrix not only provides an abundance of active surface sites for pollutant adsorption but also acts as an efficient electron acceptor, facilitating charge separation and reducing the recombination rate of photogenerated electron-hole pairs. Consequently, the non-linear kinetic analysis confirms that the functionalization of biochar with ZnO effectively boosts the photocatalytic degradation efficiency of recalcitrant pharmaceuticals like paracetamol in aqueous environments [20].

The reusability of the ZnO@BC composite was evaluated over five consecutive photocatalytic cycles under identical experimental conditions, as illustrated in Fig. 5c. The PCT removal decreased from 78.5% in the first cycle to 47.3% in the second cycle and gradually stabilized at approximately 31–32% by the fourth and fifth cycles. This pronounced decrease in performance indicates significant deactivation upon reuse. The observed loss of activity may be associated with progressive occupation or blockage of adsorption and photocatalytic sites by residual PCT and/or transformation products that are not completely removed during the washing procedure. Changes in the surface properties of the composite or partial catalyst loss during recovery may also contribute to the observed decrease in activity. However, these possible mechanisms were not directly investigated in the present study and therefore remain hypotheses. The stabilization of PCT removal at approximately 31% after the third cycle suggests that a fraction of the active sites remains functional during subsequent cycles, although with substantially reduced overall performance.

These results highlight the need for further investigation of catalyst regeneration, recovery efficiency, and deactivation mechanisms before repeated application of ZnO@BC in wastewater treatment can be considered.

The scavenging experiments showed an innovative result for ZnO application, represented in Fig. 5d. In the control system, the ZnO@BC composite displayed a notable PCT removal of 78.5 %. This superior performance is deeply tied to the structural role of biochar as an active support. When MeOH was added, the PCT removal efficiency dropped sharply to 31.2 %, confirming that hydroxyl radicals ($HO^{\bullet}$) are heavily involved in the degradation pathway, as expected for ZnO photocatalytic application. However, when ZnO is supported on BC, the carbonaceous structures can directly affect the lifetime of photogenerated holes (h^{+}), available to interact with the reactive species and generate different types of ROS. For instance, the experiment with p-BQ showed a reduction in PCT removal to 33.4 %, indicating that superoxide radicals ($O_2^{\bullet-}$) also show a co-dominance in PCT removal. This observation puts the generated ROS in the spotlight in comparison with conventional ZnO systems, which show $HO^{\bullet}$ and h^{+} as predominant active species [21,22]. Complementarily, the scavenging experiment with EDTA showed a moderate effect yet significant suppression, dropping the removal to 43.3%, indicating a significant role of photo-generated h^{+}.

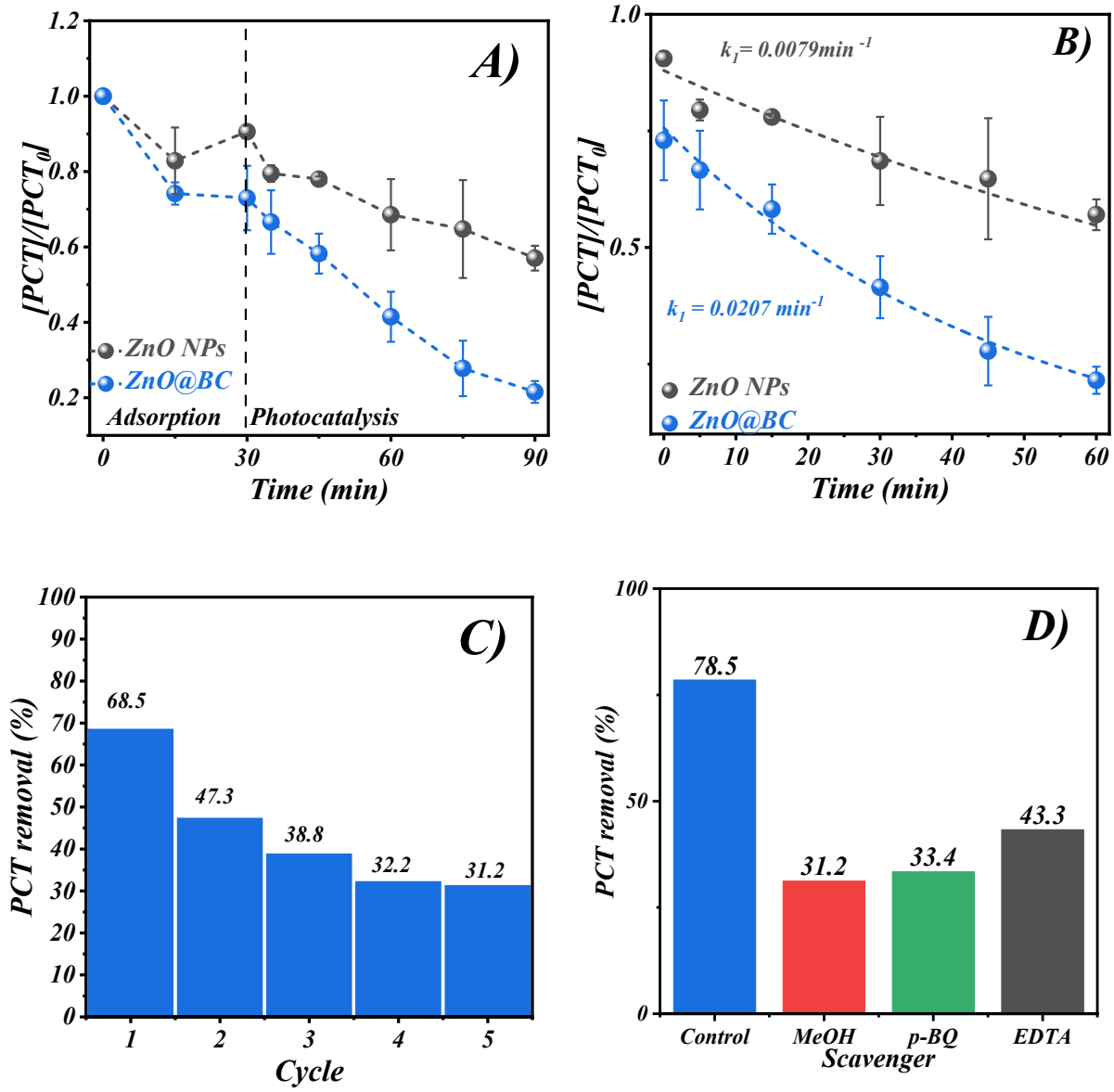


Fig. 5. Adsorption and photocatalytic degradation of PCT using commercial ZnO NPs (black line) and ZnO@BC (blue line) (A); Non-linear pseudo-first-order kinetic fitting for photocatalytic degradation (R^2=0.89725for commercial ZnO NPs and 0.99163for ZnO@BC) (B); PCT removal efficiency over five consecutive photocatalytic cycles using ZnO@BC.(C); Effect of radical scavengers MeOH, *p*-BQ and EDTA) on PCT removal efficiency by ZnO@BC (D). Experimental conditions: [PCT]= 1.0 mg L^{-1}, [catalyst]= 0.25 g L^{-1}.

Chromatographic analysis, presented in Fig. 6, corroborates the partial mineralization of PCT obtained from inorganic carbon analysis (about 32% of total PCT concentration), as seen in Fig. 6b with appearing chromatographic signals at 2.0, 2.6 and 3.6 min, as represented in the inset within the figure. These signals can be associated with UV-responsive fragments of the PCT framework remaining in the aqueous phase. Complementarily, the adsorption of PCT

and other organic fragments is plausible due to the surface characterization of the BC@ZnO composite, which resulted in a specific surface area of 74.15 m^2 g^{-1}, and the contribution of the micropores to the surface properties.

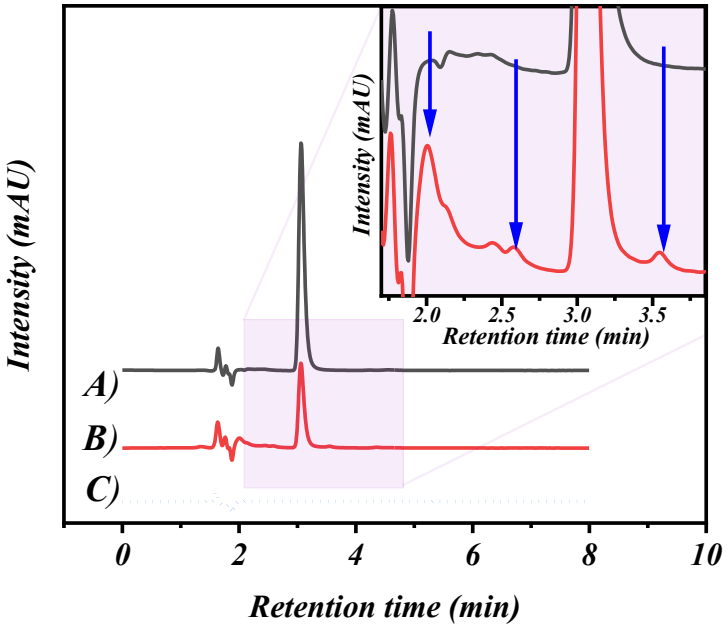


Fig. 6. HPLC-DAD profiles of PCT aqueous solutions: (A) initial PCT concentration (1.0 mg L^{-1}) prior to photocatalytic degradation, (B) remaining solution after 60 min of light irradiation in the presence of ZnO@BC and (C) blank control (ultrapure water). The inset provides a magnified view of the baseline region (1.8–3.8 min), highlighting the degradation of the primary PCT peak (~3.1 min) and the emergence of light-absorbing intermediate oxidation byproducts at retention times of 2.0, 2.6, and 3.6 min (indicated by blue arrows).

To contextualize the photocatalytic performance of the synthesized ZnO@BC composite, a comparative analysis with recently reported biochar-supported ZnO photocatalysts for pharmaceutical and organic pollutant degradation is presented in Table 4.

Table 4. Photodegradation performance of biochar-ZnO-based materials on organic contaminant removal.

Photocatalyst	Biochar Precursor	Removal percentage	Target contaminant	Catalyst dosage	k (min^{-1})	Reference
ZnO@BC	Sugar cane bagasse	78.5%	paracetamol	0.25 g L^{-1}	0.02065	This work
Lavender-derived ZnO/Biochar	Lavender	75.2% (paracetamol) 62,8% (doxycycline)	Paracetamol and doxycycline	1.0 g L^{-1}	0.01130	[23]
SB450	sugarcane bagasse	90.8% (methyl orange) 99.3% (sulfamethoxazole)	methyl orange sulfamethoxazole	1.0 g L^{-1}	Not reported	[24]
BCZ-3	*Calotropis gigantea* leaves	98.5%	ciprofloxacin	1.0 g L^{-1}	0.09341	[25]
RFL-ZnO	*Ficus elástica* leaves	90.0%	levofloxacin	0.45 g L^{-1}	0.01286	[26]
ZBC	*Phragmites australis*	92.4%	doxycycline	0.50 g L^{-1}	0.04314	[27]
ZnO/COFF	Biowaste from brewed coffee	95.0%	ibuprofen	0.50 g L^{-1}	Not reported	[28]

A-0.3 (T-700)	Peanut shell	97.08%	tetracycline	1.0 g L^{-1}	0.02300	[29]

The ZnO@BC composite demonstrated a high removal efficiency (78.5%) and a remarkable apparent kinetic rate constant (k = 0.02065 min^{-1}) for paracetamol removal. Crucially, this performance was achieved using a significantly lower catalyst dosage (0.25 g L^{-1}) compared to the majority of literature studies, which typically rely on higher loadings ranging from 0.45 to 1.0 g L^{-1}. For instance, relative to another paracetamol-targeting system (Lavender-derived ZnO/Biochar), the present ZnO@BC composite achieved a higher removal rate and nearly double the kinetic rate constant (0.02065 vs. 0.01130 min^{-1}) while utilizing only one-fourth of the catalyst mass.

Furthermore, while systems using higher dosages such as BCZ-3 (1.0 g L^{-1}) or A-0.3 (1.0 g L^{-1}) achieved higher total removal percentages for ciprofloxacin and tetracycline, their high catalyst load increases turbidity, potential light-shielding effects, and overall operational costs. The superior mass-normalized reactivity of the ZnO@BC composite highlights the synergistic effect between the sugarcane bagasse-derived biochar matrix and the active ZnO nanoparticles, which facilitates optimized light absorption, reduced deep-trap charge recombination (E_U = 49.3 meV), and active charge transport even at low catalyst loadings

3.4 Scavenging tests and mechanistic deduction

The scavenging results provide indirect evidence regarding the reactive species involved in PCT transformation over ZnO@BC. Under irradiation, the ZnO semiconductor can generate electron–hole pairs, as represented by Eq. (7). The photogenerated holes may participate in the oxidation of adsorbed water molecules or hydroxyl species to produce hydroxyl radicals (•OH), as represented in Eq. (8). Meanwhile, photogenerated electrons can react with dissolved oxygen to form superoxide radicals ($O_2^{\bullet-}$), as represented in Eqs. (9) and (10) [20-22,30].

$$ZnO@BC + hv \rightarrow h^+(ZnO) + e^-(ZnO) \quad (7)$$

$$H_2O + h^+(surface\ ZnO@BC) \rightarrow HO^\bullet + H^+ \quad (8)$$

$$h^+(ZnO) + e^-(ZnO) \rightarrow h^+(surface\ ZnO@BC) + e^-(trapped\ BC) \quad (9)$$

$$O_2 + e^-(trapped) \rightarrow O_2^{\bullet-} \quad (10)$$

The scavenging experiments with EDTA showed the contribution of h^+ in the photocatalytic systems, pointing that direct hole (h^+) oxidation also occur. PCT molecules can interact directly with h^+ sites by charge transfer between photogenerated holes and the adsorbed organic structure of PCT, as represented by Eq. 11.

$$PCT + h^+(ZnO) \rightarrow degradation\ products \quad (11)$$

Radical trapping experiments were performed using MeOH, *p*-benzoquinone and EDTA were used in scavenging agents for hydroxyl radicals ($HO^{\bullet}$), superoxide radicals ($O_2^{\bullet-}$) and photogenerated holes (h^+) scavenging (Fig. 5d). As depicted in Fig. 5d, the addition of both MeOH and p-BQ induced a drastic suppression of PCT removal efficiency from 78.5% (control) down to 31.2% and 33.4%, respectively, whereas EDTA caused a moderate inhibition (43.3 %). These quenching trends confirm that $HO^{\bullet}$ and $O_2^{\bullet-}$ function as the primary reactive oxygen species (ROS) driving the photocatalytic degradation, while h^+ plays a secondary supportive role. This synergistic ROS generation aligns seamlessly with the established electronic band structure: photogenerated holes residing in the valence band of ZnO (E_{VB} = +2.88 V vs. NHE) possess a sufficiently positive potential to drive the direct oxidation of adsorbed H_2O/OH^- into $HO^{\bullet}$ radicals (+2.38 V vs. NHE). Concurrently, photoexcited electrons transferred via carbon-induced intra-gap states to the conductive π-conjugated network of the biochar matrix undergo efficient interfacial reaction with dissolved O_2 to yield $O_2^{\bullet-}$ radicals. The biochar matrix acts as an effective electron trap, hindering charge recombination and prolonging carrier lifetimes, which sustains the continuous, high-yield production of both $HO^{\bullet}$ and $O_2^{\bullet-}$ active species.

In summary, the scavenging profile demonstrates that the biochar support does not merely hold the semiconductor mechanically, but can participate in charge separation and transport, triggering an interconnected mechanism driven simultaneously by $HO^{\bullet}$, $O_2^{\bullet-}$ and h^+ [7,30]. The PCT molecules can primarily be adsorbed onto ZnO@BC surface (Fig. 7a) due BC adsorptive properties. Secondarily, PCT molecules can interact with both radicals ($HO^{\bullet}$ and $O_2^{\bullet-}$) or directly with the photogenerated holes (h^+) promotes its degradation, through advanced oxidation and reduction processes, as represented in Fig. 7b.

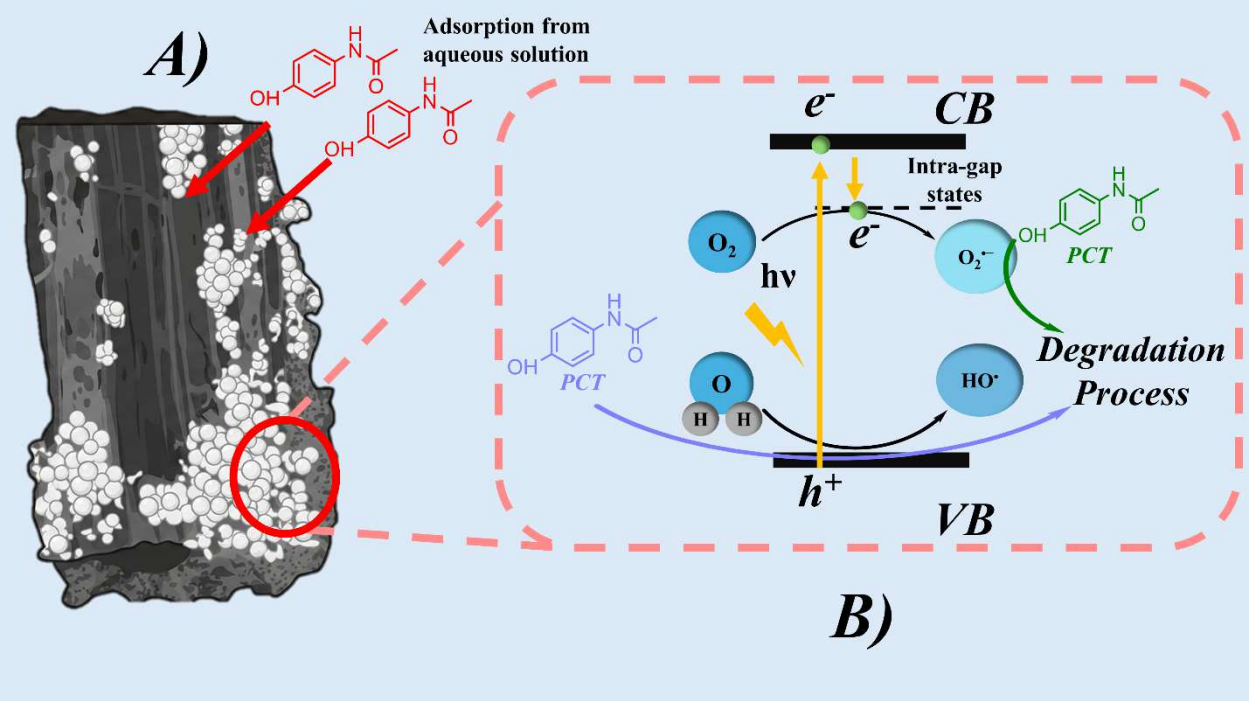


Fig 7. Proposed radical generation steps and in plausible interactions between PCT and ZnO@BC: through adsorption processes (A) and in photocatalysis with PCT and ROS (green arrow) and PCT with h^+ (blue arrow) (B).

4 CONCLUSIONS

ZnO-functionalized sugarcane-bagasse biochar (ZnO@BC) was successfully synthesized and characterized as a hybrid photocatalytic material for the removal of paracetamol (PCT) from aqueous solution. Structural and surface characterization confirmed the presence of crystalline wurtzite ZnO associated with the biochar matrix, while the textural properties indicated a porous structure with a BET surface area of 74.15 m^2g^{-1}. Optical and photoelectrochemical analyses further indicated that the ZnO@BC interface modifies the electronic and charge-transport properties of ZnO, with the EIS results showing increased low-frequency conductance under illumination.

Under the investigated conditions, ZnO@BC achieved 78.5% removal of the parent PCT compound, outperforming commercial ZnO under the same experimental conditions. The photocatalytic removal kinetics were well described by a pseudo-first-order model. Scavenger experiments indicated that hydroxyl radicals (HO•),

superoxide radicals ($O_2^{\bullet-}$), and photogenerated holes contribute to PCT removal, supporting the involvement of both reactive oxygen species and direct hole-mediated oxidation pathways.

Inorganic carbon analysis indicated approximately 32% mineralization, corroborated with HPLC-DAD chromatograms with appearing peaks after photocatalytic experiments, demonstrating that the disappearance of the parent PCT compound was accompanied by partial transformation rather than complete mineralization. The enhanced photocatalytic performance is consistent with the combined effects of PCT adsorption on the biochar matrix, the porous structure of the composite, and improved photoinduced charge transport at the ZnO/biochar interface.

Although ZnO@BC retained photocatalytic activity after repeated use, the marked decrease in removal efficiency over successive cycles indicates that catalyst deactivation remains an important limitation. Further studies should therefore investigate regeneration strategies, catalyst deactivation mechanisms, and the identification and toxicity assessment of transformation products, as well as evaluate the performance of ZnO@BC in more complex water matrices and real wastewater.

ACKNOWLEDGEMENTS

The authors would like to thank the Federal University of Itajubá (UNIFEI), the Physics and Chemistry Institute (IFQ), the National Council for Scientific and Technological Development (CNPq), the Research Support Foundation of Minas Gerais (FAPEMIG) and the National Council for Improvement of Higher Education (CAPES).

FUNDING

The research was supported by the National Council for Improvement of Higher Education (scholarship process number 88887.903838/2023-00) and by the National Council for Scientific and Technological Development (scholarship process number 139696/2025-3).

DATA AVAILABILITY STATEMENT

The data will be made available on request.

AI DISCLOSURE STATEMENT

During the preparation of this work, the authors used Grammarly (v.1.2.236.1843) in order to improve the readability and language of the text. After using this tool, the authors reviewed and edited the content as needed and take full responsibility for the content of the publication. Google Gemini was used in order to conceptualize the initial draft of Fig. 7.

CONFLICT OF INTEREST

The Authors declare that no competing financial interest or personal relationships is known.

REFERENCES

1. Mohamed KM, Benitto JJ, Vijaya JJ, Bououdina M (2023) Recent Advances in ZnO-Based Nanostructures for the Photocatalytic Degradation of Hazardous, Non-Biodegradable Medicines. Crystals 13 (2). doi:10.3390/cryst13020329
2. Yadav D, Rangabhashiyam S, Verma P, Singh P, Devi P, Kumar P, Hussain CM, Gaurav GK, Kumar KS (2021) Environmental and health impacts of contaminants of emerging concerns: Recent treatment challenges and approaches. Chemosphere 272:129492. doi:10.1016/j.chemosphere.2020.129492
3. Zhu C, Wang X (2025) Nanomaterial ZnO Synthesis and Its Photocatalytic Applications: A Review. Nanomaterials (Basel) 15 (9). doi:10.3390/nano15090682
4. Morin-Crini N, Lichtfouse E, Liu G, Balaram V, Ribeiro ARL, Lu Z, Stock F, Carmona E, Teixeira MR, Picos-Corrales LA, Moreno-Piraján JC, Giraldo L, Li C, Pandey A, Hocquet D, Torri G, Crini G (2022) Worldwide cases of water pollution by emerging contaminants: a review. Environmental Chemistry Letters 20 (4):2311-2338. doi:10.1007/s10311-022-01447-4
5. Hu H, Sun L, Gao Y, Wang T, Huang Y, Lv C, Zhang YF, Huang Q, Chen X, Wu H (2020) Synthesis of ZnO nanoparticle-anchored biochar composites for the selective removal of perrhenate, a surrogate for pertechnetate, from radioactive effluents. J Hazard Mater 387:121670. doi:10.1016/j.jhazmat.2019.121670

6. Tharayil JM, Chinnaiyan P, Ramasamy B, Sathasivan A (2025) Biogenic synthesis of Cu/ZnO functionalized biochar composite: A sustainable approach for visible light-photocatalytic degradation. Environmental Technology & Innovation 39. doi:10.1016/j.eti.2025.104337
7. Weidner E, Karbassiyazdi E, Altaee A, Jesionowski T, Ciesielczyk F (2022) Hybrid Metal Oxide/Biochar Materials for Wastewater Treatment Technology: A Review. ACS Omega 7 (31):27062-27078. doi:10.1021/acsomega.2c02909
8. Xu R, Li M, Zhang Q (2022) Collaborative optimization for the performance of ZnO/biochar composites on persulfate activation through plant enrichment-pyrolysis method. Chemical Engineering Journal 429. doi:10.1016/j.cej.2021.132294
9. Moezzi A, Cortie M, McDonagh A (2016) Transformation of zinc hydroxide chloride monohydrate to crystalline zinc oxide. Dalton Trans 45 (17):7385-7390. doi:10.1039/c5dt04864h
10. Qu S, Hadjittofis E, Malaret F, Hallett J, Smith R, Campbell KS (2023) Controlling simonkolleite crystallisation via metallic Zn oxidation in a betaine hydrochloride solution. Nanoscale Adv 5 (9):2437-2452. doi:10.1039/d3na00108c
11. Liu Z, Liu L, He S, Chen Y, Zhang S, Dong X, Chang Z, Duan X (2025) Quenching should be used with caution to evaluate the role of reactive oxygen species in the degradation of pollutants by electro-advanced oxidation technology. Process Safety and Environmental Protection 195. doi:10.1016/j.psep.2025.106823
12. Carlsson C, Fégeant B, Svensson E, Wiklund L, Jonsson M (2022) On the Selectivity of Radical Scavengers Used To Probe Hydroxyl Radical Formation in Heterogeneous Systems. The Journal of Physical Chemistry C 126 (30):12435-12440. doi:10.1021/acs.jpcc.2c01834
13. Cousy S, Gorodylova N, Svoboda L, Zelenka J (2017) Influence of synthesis conditions over simonkolleite/ZnO precipitation. Chemical Papers 71 (12):2325-2334. doi:10.1007/s11696-017-0226-4
14. Perillo P. M. AMN, Rodríguez D. F. (2018) Studies on the Growth Control of ZnO

Nanostructures synthesized by

the Chemical Method. Revista Matéria 23. doi:https://doi.org/10.1590/S1517-707620180002.0467
15. Tang M, Snoussi Y, Bhakta AK, El Garah M, Khalil AM, Ammar S, Chehimi MM (2023) Unusual, hierarchically structured composite of sugarcane pulp bagasse biochar loaded with Cu/Ni bimetallic nanoparticles for dye removal. Environ Res 232:116232. doi:10.1016/j.envres.2023.116232
16. Derbali L (2022) Electrical and Optoelectronic Properties Enhancement of n-ZnO/p-GaAs Heterojunction Solar Cells via an Optimized Design for Higher Efficiency. Materials (Basel) 15 (18). doi:10.3390/ma15186268
17. Jonscher AK (1977) The 'universal' dieletric response. Nature 263. doi:DOI: 10.1038/267673a0
18. Boukamp BA (1995) A Linear Kronig-Kramers Transform Test for Immittance Data Validation. Journal of Electrochemical Society 142 (6):1885 - 1894. doi:DOI: 10.1149/1.2044210
19. Mohan D, Sarswat A, Ok YS, Pittman CU, Jr. (2014) Organic and inorganic contaminants removal from water with biochar, a renewable, low cost and sustainable adsorbent--a critical review. Bioresour Technol 160:191-202. doi:10.1016/j.biortech.2014.01.120
20. Mian MM, Liu G (2018) Recent progress in biochar-supported photocatalysts: synthesis, role of biochar, and applications. RSC Adv 8 (26):14237-14248. doi:10.1039/c8ra02258e
21. Mahajan M, Kumar S, Gaur J, Kaushal S, Dalal J, Singh G, Misra M, Ahlawat DS (2025) Green synthesis of ZnO nanoparticles using Justicia adhatoda for photocatalytic degradation of malachite green and reduction of 4-nitrophenol. RSC Adv 15 (4):2958-2980. doi:10.1039/d4ra08632e
22. Ahmed ZM, Allam AA, El-Sayed MI, El-Gaied IMA, Salama Y, Rudayni HA, Zoubi WA, Abukhadra MR (2026) Visible-light photocatalytic mineralization of 4-Chlorophenol over ZnO-loaded sulfonated carbonaceous bentonite: kinetic analysis, pathway elucidation, and catalyst reusability. Sci Rep 16 (1):5319. doi:10.1038/s41598-026-35956-x
23. Krasteva L, Sandov O, Ivanova D, Naydenova I, Kaneva N (2026) Lavender-Derived ZnO/Biochar for Photocatalytic Degradation of Doxycycline and Paracetamol. Processes 14 (6). doi:10.3390/pr14060881
24. Goncalves MG, da Silva Veiga PA, Fornari MR, Peralta-Zamora P, Mangrich AS, Silvestri S (2020) Relationship of the physicochemical properties of novel ZnO/biochar composites to their efficiencies in the degradation of sulfamethoxazole and methyl orange. Sci Total Environ 748:141381. doi:10.1016/j.scitotenv.2020.141381
25. Amir M, Fazal T, Iqbal J, Din AA, Ahmed A, Ali A, Razzaq A, Ali Z, Rehman MSU, Park Y-K (2022) Integrated adsorptive and photocatalytic degradation of pharmaceutical micropollutant, ciprofloxacin employing biochar-ZnO composite photocatalysts. Journal of Industrial and Engineering Chemistry 115:171-182. doi:10.1016/j.jiec.2022.07.050

26. Sudarsan S, Shetty SA, Vinayagam R, Selvaraj R (2026) Mesoporous ZnO–biochar composite with enhanced sunlight photocatalytic activity toward levofloxacin degradation. Materials Technology 41 (1). doi:10.1080/10667857.2026.2658620
27. Tuoi NT, Nguyet BTM, Tuyen TN, Khac Lieu P, Khieu DQ, Van Hung N (2024) Dispersion of ZnO or TiO2 nanoparticles onto P. australis stem-derived biochar for highly efficient photocatalytic removal of doxycycline antibiotic under visible light irradiation. Materials Research Express 11 (9). doi:10.1088/2053-1591/ad7448
28. Gonçalves NPF, Lourenço MAO, Baleuri SR, Bianco S, Jagdale P, Calza P (2022) Biochar waste-based ZnO materials as highly efficient photocatalysts for water treatment. Journal of Environmental Chemical Engineering 10 (2). doi:10.1016/j.jece.2022.107256
29. Yu S, Zhou J, Ren Y, Yang Z, Zhong M, Feng X, Su B, Lei Z (2023) Excellent adsorptive-photocatalytic performance of zinc oxide and biomass derived N, O-contained biochar nanocomposites for dyes and antibiotic removal. Chemical Engineering Journal 451. doi:10.1016/j.cej.2022.138959
30. Cui J, Zhang F, Li H, Cui J, Ren Y, Yu X (2020) Recent Progress in Biochar-Based Photocatalysts for Wastewater Treatment: Synthesis, Mechanisms, and Applications. Applied Sciences 10 (3). doi:10.3390/app10031019

Supplementary Files

This is a list of supplementary files associated with this preprint. Click to download.

- SupplementaryMaterial.docx